

Tracking the spatio-temporal evolution of foreshocks preceding the Mw 6.3 2009 L'Aquila Earthquake

Leoncio Cabrera¹, Piero Poli², and William Benjamin Frank³

¹ISTerre Institut des Sciences de la Terre, CNRS, Université Grenoble Alpes

²Université Grenoble-Alpes, Isterre Laboratory, CNRS

³Massachusetts Institute of Technology

November 24, 2022

Abstract

How faulting processes lead to a large earthquake is a fundamental question in seismology. To better constrain this pre-seismic stage, we create a dense seismic catalog via template matching to analyze the precursory phase of the Mw 6.3 L'Aquila earthquake that occurred in central Italy in 2009. We estimate several physical parameters in time, such as the coefficient of variation, the seismic moment release, the effective stress drop, and analyze spatio-temporal patterns to study the evolution of the sequence and the earthquake interactions. We observe that the precursory phase experiences multiple accelerations of the seismicity rate that we divide into two main sequences with different signatures and features: the first part exhibits weak earthquake interactions, quasi-continuous moment release, slow spatial migration patterns, and a lower effective stress drop, pointing to aseismic processes. The second sequence exhibits strong temporal clustering, rapid spatial expansion of the seismicity and larger effective stress drop typical of a stress transfer process. We interpret the differences in the seismicity behavior between the two sequences as distinct physical mechanisms that are controlled by different physical properties of the fault system. We conclude that the L'Aquila earthquake is preceded by a complex preparation, made up of different physical processes taking place over different time scales on faults with different physical properties.

Tracking the spatio-temporal evolution of foreshocks preceding the Mw 6.3 2009 L'Aquila Earthquake

Leoncio Cabrera^{1*}, Piero Poli¹ and William B. Frank²

¹ISTerre Institut des Sciences de la Terre, CNRS, Université Grenoble Alpes, France

²Department of Earth, Atmospheric and Planetary Sciences, Massachusetts Institute of Technology, Cambridge, MA, USA

Corresponding author: Leoncio Cabrera (leoncio.cabrera@univ-grenoble-alpes.fr)

Université Grenoble Alpes, ISTerre CS 40700 38058, GRENOBLE Cedex 9

Key Points:

- We build a new, denser catalog of foreshocks before the M6.3 L'Aquila earthquake
- We reveal a complex two stages evolution of the precursory seismicity
- The precursory seismicity is driven by different processes as external forcing and stress interaction

Abstract

How faulting processes lead to a large earthquake is a fundamental question in seismology. To better constrain this pre-seismic stage, we create a dense seismic catalog via template matching to analyze the precursory phase of the Mw 6.3 L'Aquila earthquake that occurred in central Italy in 2009. We estimate several physical parameters in time, such as the coefficient of variation, the seismic moment release, the effective stress drop, and analyze spatio-temporal patterns to study the evolution of the sequence and the earthquake interactions. We observe that the precursory phase experiences multiple accelerations of the seismicity rate that we divide into two main sequences with different signatures and features: the first part exhibits weak earthquake interactions, quasi-continuous moment release, slow spatial migration patterns, and a lower effective stress drop, pointing to aseismic processes. The second sequence exhibits strong temporal clustering, rapid spatial expansion of the seismicity and larger effective stress drop typical of a stress transfer process. We interpret the differences in the seismicity behavior between the two sequences as distinct physical mechanisms that are controlled by different physical properties of the fault system. We conclude that the L'Aquila earthquake is preceded by a complex preparation, made up of different physical processes taking place over different time scales on faults with different physical properties.

Plain Language Summary

In this work we study the seismicity before the Mw 6.3 2009 L'Aquila earthquake. We first catalog almost 5000 events from the continuous seismic record. We then analyze the spatio-temporal evolution of this sequence through several physical parameters. We observe that the sequence is

37 divided in two main sequences. Our results indicate that several different physical mechanisms
38 (e.g., aseismic deformation, stress transfer due to earthquake interactions) and potential
39 heterogeneities in the fault system (e.g., distance between seismic regions) controlled how the
40 earthquake sequence played out. Our observations show a complex spatiotemporal evolution
41 during the precursory phase and challenge classic fault models that explain earthquake initiation
42 as a process along a homogenous planar fault.

43 **1 Introduction**

44 The characterization of the physical processes occurring before major earthquakes is a
45 fundamental challenge in seismology. So far, physical models have been proposed to explain the
46 processes that lead to large seismic events, including cascade, pre-slip, and progressive or
47 migratory localization (Ellsworth & Beroza, 1995; McLaskey, 2019; Kato & Ben-Zion, 2020).
48 Which one of these mechanisms best represents the physics of the precursory phase of earthquakes
49 is still under debate.

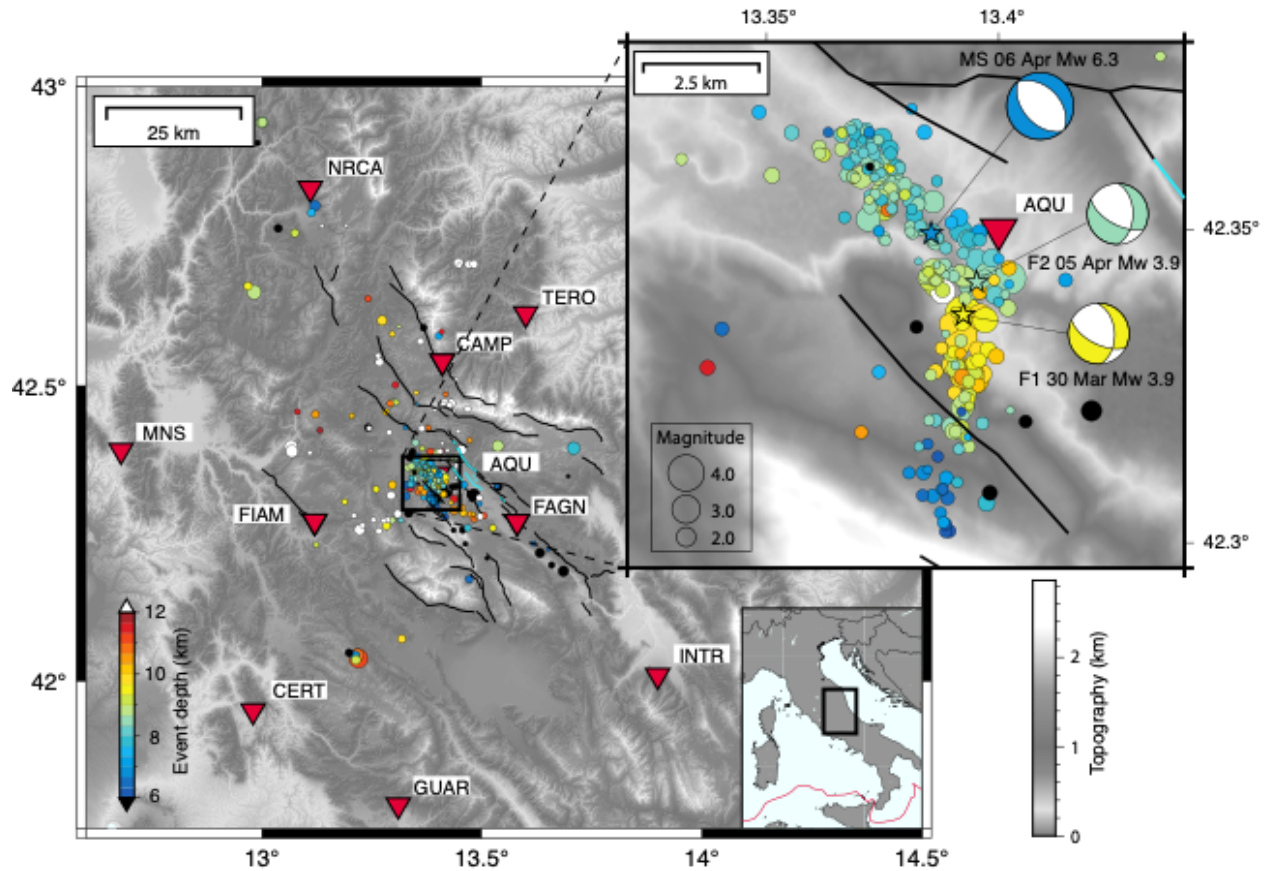
50 One of the most powerful tools to study the physical processes taking place before the
51 occurrence of significant earthquakes are foreshocks: small earthquakes that precede some large
52 mainshocks (Dodge et al., 1996; Bouchon et al., 2013). Foreshocks were first observed more than
53 a century ago (Omori, 1908). Since then, many laboratory studies have focused on the precursory
54 moment release (Acosta et al., 2019), aseismic slip and stress changes (McLaskey & Kilgore,
55 2013; McLaskey & Lockner, 2014) and other characteristics of the foreshocks during the initiation
56 of laboratory earthquakes (McLaskey, 2019 and references therein). In addition, direct
57 seismological observations in different seismotectonic settings such as strike-slip faults (e.g.,
58 Dodge et al., 1995, 1996; Bouchon et al., 2011; Chen & Shearer, 2013; Ellsworth & Bulut, 2018;
59 Tape et al., 2018; Yoon et al., 2019; Shelly, 2020; Durand et al., 2020), subduction zones (Kato et
60 al., 2012; Bouchon et al., 2013; Ruiz et al., 2014, 2017), and extensional regimes (Sugan et al.,
61 2014; Sánchez-Reyes et al., 2021) have been carried out to assess which model best explains the
62 occurrence of foreshocks and the physical processes occurring during the precursory phase of large
63 earthquakes. More recently, some studies have taken advantage of high-resolution detection
64 methods such as template matching and/or machine learning (e.g., Gardonio et al., 2019; Ross et
65 al., 2019; Yoon et al., 2019; Durand et al., 2020; Shelly, 2020; Sánchez-Reyes et al., 2021) and
66 the availability of better field data (e.g., more stations near faults. See Savage et al., 2017; Tape et
67 al., 2018; Meng and Fan, 2021; Simon et al., 2021) to study foreshocks. These studies reveal an
68 increased spatiotemporal complexity (i.e., fault interactions, volumetric processes, heterogeneous
69 fault properties) of the processes taking place before large earthquakes. This complexity, mainly
70 revealed by foreshocks patterns, is hard to reconcile with a single physical explanation of the
71 precursory phase (cascade, pre-slip or progressive localization). In addition, the observed
72 foreshocks patterns challenge the actual laboratory scale and theoretical models, which treat
73 earthquake initiation as a process along a homogenous planar fault (Dieterich, 1992; Marone,
74 1998; Liu & Rice, 2005; Rubín & Ampuero, 2005) or a combination of several planar fault
75 segments (Shimizu et al., 2021), although some cases with non-planar fault geometry exist (e.g.,
76 Zhang et al., 2014; Dutta et al., 2021).

77 To gain insight about the ongoing physical processes occurring near to the nucleation
78 region, before a large earthquake, we study the Mw 6.3 2009 L'Aquila earthquake and its foreshock
79 sequence. This event, which struck central Italy on 6 April 2009 (01:32 UTC) causing damage and
80 fatalities, was preceded by more than 500 small ($M > 0.5$) earthquakes (Chiaraluce et al., 2011).
81 Based on the locations of the events, Chiaraluce et al. (2011) reported that the sequence of

82 foreshocks took place in two different faults: (1) a main fault, where the mainshock (Fig. 1) occurs
83 on 6 April 2009, that hosts most of the seismicity occurring from the beginning of January until
84 30 March; and (2) an antithetic fault that is activated on 30 March 2009 by a Mw 3.9 foreshock
85 (hereafter F1, Fig. 1). On 5 April 2009 (five hours before the mainshock), the seismicity migrates
86 back to the main fault after the occurrence of another Mw 3.9 foreshock (hereafter F2, Fig. 1,
87 Chiaraluce et al., 2011). The co-seismic rupture took place in the Paganica fault (Falcucci et al.,
88 2009; Cheloni et al., 2010), generating exposed ground deformation (Falcucci et al., 2009; Boncio
89 et al., 2010) and maximum surface displacements of 8.1 cm and 16.5 cm in the vertical and
90 horizontal directions, respectively (Cheloni et al., 2010). Joint inversion using GPS, strong motion,
91 and Synthetic Aperture Radar (SAR) data indicate that the maximum slip on the fault is of the
92 order of 1.4 m (Cirella et al., 2012). According to different rupture models (e.g., Cirella et al.,
93 2009, 2012; Cheloni et al., 2010; Scognamiglio et al., 2010), the slip was concentrated in two main
94 asperities: a small patch updip from the hypocenter, and a second, larger asperity located to the
95 southeast along strike. In this context, the foreshocks were located at the base of the activated fault
96 plane in a region where almost no slip occurred during the mainshock rupture (Valoroso et al.,
97 2013).

98 Here we complement previous studies of foreshocks of the L'Aquila earthquake
99 (Chiaraluce et al., 2011; Valoroso et al., 2013; Sukan et al., 2014; Vuan et al., 2018), by estimating
100 quantitative parameters of the spatiotemporal evolution of the foreshocks sequence. We focus on
101 an area of 10 km x 10 km surrounding the epicenter (Fig. 1). We then densify the catalog of
102 seismicity before the L'Aquila earthquake by using template matching (Gibbons & Ringdal, 2006)
103 to scan 6 months of data before the main shock. We use a frequency band between 5-30 Hz. The
104 inclusion of high frequencies (>20Hz) compared to previous studies (Sukan et al., 2014; Vuan et
105 al., 2018) permitted us to detect more small events ($\sim M < 1.0$), which are best captured at high
106 frequency. Our final catalog that covers from 6 October 2008 to 6 April 2009, contains 4978
107 events, with the first event occurring on 3 January 2009. No seismicity was detected from 6
108 October 2008 to 2 January 2009.

109 Using this new catalog, we analyze the seismic sequence of foreshocks by tracking the time
110 evolution of temporal clustering (earthquake interactions), seismic moment release, and effective
111 stress drop. We also study the spatio-temporal evolution of the events to better characterize the
112 precursory phase of the L'Aquila earthquake. Based on these results, we discuss the physical
113 mechanisms that controls the foreshock sequence, ultimately leading to the mainshock.



114

115 **Figure 1:** Location map for the L'Aquila earthquake showing the precursory seismicity detected by Chiaraluce et al. (2011); our
 116 267 template events are drawn from this earthquake catalog and are shown in the zoom. The broadband stations we analyzed are
 117 shown by the red triangles. Black and cyan thin lines represent traces of the active mapped faults and co-seismic surface ruptures,
 118 respectively (Boncio et al., 2010). Upper-right zoom: 267 events used as templates to scan continuous data color-size coded
 119 according to depth and magnitude, respectively. Beachballs (compressional quadrants in colors) represent source mechanisms
 120 (reported by INGV) for the mainshock (MS 6 April) and the two foreshocks Mw 3.9 one week (F1 30 March) and five hours (F2
 121 5 April) before it, discussed in this study. All of them correspond to normal (extensional) mechanisms.

122 2 Extending the Seismic Catalog

123 We apply template matching (Gibbons & Ringdal, 2006) to continuous seismic data
 124 collected by the Istituto Nazionale di Geofisica e Vulcanologia (INGV) from 6 October 2008 to 6
 125 April 2009 (6 months). We use 10 broadband three-component stations (red triangles in Fig. 1)
 126 from the Italian Seismic Network (INGV Seismological Data Centre, 2006) and the Mediterranean
 127 Very Broadband Seismographic Network (MedNet Project Partner Institutions, 1990). Data was
 128 continuously recorded at a sampling rate of 100 Hz. Before using the data to study earthquakes,
 129 we performed a visual inspection of the spectrograms (Fig. S1), to find the frequency range which
 130 is less affected by the strong anthropogenic noise existing in the Apennines (Poli et al., 2020).
 131 From this analysis we choose to filter the continuous data from 5 to 30 Hz. The dataset was then
 132 organized into 24-hour continuous files with all gaps filled with zeros.

133 We consider 512 foreshocks reported by Chiaraluce et al. (2011) as potential templates,
 134 which have a relative horizontal and vertical location errors about 40 m and 80 m, respectively
 135 (Chiaraluce et al., 2011). We identify the highest-quality events by estimating the signal-to-noise
 136 ratio (SNR) of each event as the ratio between the RMS velocity during the first 3 s of the P and S

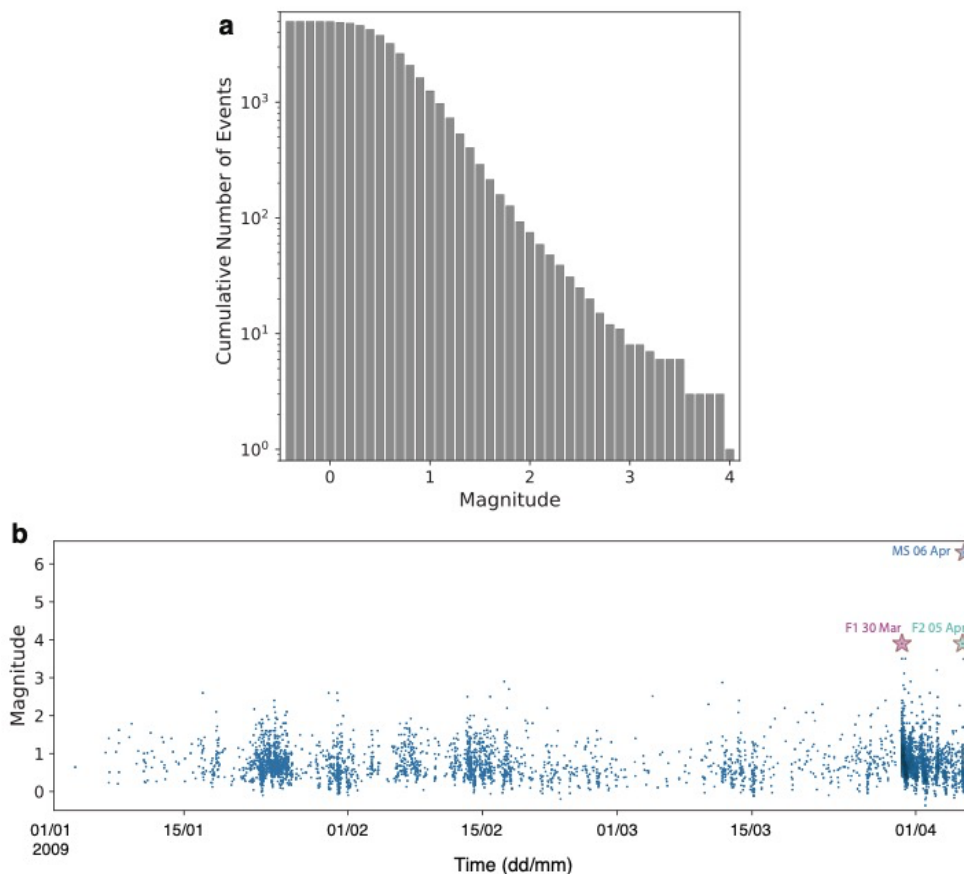
137 waves (for vertical and horizontal components, respectively), and the RMS velocity during a 3 s
138 of noise before the P and S wave arrival times (e.g., Frank et al., 2017; Cabrera et al., 2021). A
139 signal is retained as a final template if it has a $\text{SNR} \geq 2$ for at least 12 components. We finally
140 retained 267 template event waveforms (inset in Fig. 1), defined as the 3.5 s time windows that
141 starts 0.5 s before the P- and S-wave arrivals at each station for the vertical and horizontal
142 components, respectively, and filtered in an identical manner to the continuous data (bandpassed
143 between 5-30 Hz). The template waveforms are then correlated against a sliding window of
144 continuous data using a GPU-architecture and the Fast Matched Filter algorithm (Beaucé et al.,
145 2018) to obtain daily correlation functions. We search sample-by-sample considering a detection
146 threshold that is 12 times the median absolute deviation (MAD) of the correlation function
147 averaged over all stations and channels to detect events significantly similar to the template. We
148 defined this detection threshold to minimize the occurrence of false detections by first scanning
149 the continuous data using the templates flipped in time (see an example in Fig. S2). With this
150 approach the data are scanned using non-physical and acausal templates unlikely to detect
151 anything, but with the same frequency content as the original templates. We test the number of
152 detections using $N \times \text{MAD}$ with N in the range 9-12 (see Fig. S3), and we decided to use $N=12$ as
153 this threshold provides only one false detection during the whole period of time (6 October 2008
154 to 6 April 2009). To remove double detections over the same time window, we merge consecutive
155 detections with differential times less than 4 s; we keep the detection with the largest average
156 correlation coefficient as the final detection.

157 We estimate the magnitude of each new event by computing the mean P- and S-wave
158 amplitude ratio between the template event and the detection over the components with a $\text{SNR} \geq$
159 2. Using the template event's catalog magnitude as a reference, the magnitude of a detected event
160 is determined, assuming that a ratio of 10 of the amplitude ratio corresponds to a variation of one-
161 unit of magnitude (e.g., Peng & Zhao, 2009; Frank et al., 2017; Cabrera et al., 2021).

162 We further attempt to relocate the newly detected seismicity, respect to the templates. For
163 this scope, we use pair-wise cross-correlation (CC) between each template and its detections, to
164 measure differential delay times. For each event pair, we use waveforms windows of 2 s starting
165 1 s before the P- and S-waves, respectively. We then relocate each family of detections (a template
166 and its detections) with GrowClust (Trugman & Shearer, 2017). An event pair is only used if its
167 cross-correlation coefficient (r_{min}) is ≥ 0.6 with a maximum source-receiver distance (del_{max})
168 of 80 km. We also considered a maximum root-mean-square differential time residual for a
169 proposed cluster merger to be allowed during the relocation algorithm (rms_{max}) ≤ 0.2 (see
170 Trugman and Shearer, 2017. For more details). This procedure resulted in 722 events relocated, or
171 $\sim 17\%$ of the original catalog (Fig. S4). Although low, this percentage is not surprising given the
172 configuration of the network. For example, Ross et al. (2019) relocated 38.7% of events using a
173 denser array of stations in California and Simon et al. (2021) relocated 11.6% of their catalog in
174 Switzerland, in both cases after using template matching. This data reduction is due to the fact that
175 double difference relocations rely on high quality correlations at a single station, while template
176 matching leverages an average correlation across the entire network to identify events that would
177 otherwise go unnoticed. This means that some events could be detected by template matching can
178 have relatively low correlation coefficients that are not necessarily suitable for relocation.
179 Although it is possible to increase the number of relocated events by relaxing for example the
180 r_{min} and rms_{max} parameters, we decided to rather use values similar to previous works (e.g.,
181 Trugman and Shearer, 2017; Ross et al., 2019) to prevent a degradation of the quality of the
182 relocation.

183 As small number of events can be relocated with the approach described above, the new
 184 events are considered to occur at the same hypocenter (determined by Chiaraluce et al., 2011) as
 185 the template. However, we got an estimation of the distance between the initial location of the
 186 detections and the relocated position of new detections. On average, horizontal and vertical
 187 distances between templates and new detections are in the order of 83 m and 66 m, respectively
 188 (see Figs. S5-6). These values are similar to other studies (~ 100 -200 m, Ross et al., 2019; Simon
 189 et al., 2021).

190 Our final catalog contains 4978 events with magnitude ranging from -0.4 to 3.9 (Fig. 2).
 191 We estimate the magnitude of completeness (M_c) of our catalog, using the Lilliefors test
 192 implemented by Herrmann and Marzochi (2020), which in general provides conservative values
 193 of the M_c (see examples in Herrmann and Marzochi, 2020) and allows us to ensure the stability of
 194 our further analysis. We use a binning of $\Delta M=0.01$ and we also test M_c for two significance level
 195 of $\alpha=0.05$ and $\alpha=0.01$, obtaining $M_c=0.8$ and $M_c=0.9$, respectively. As indicated by Herrmann and
 196 Marzochi (2020), choosing $\alpha=0.01$ is conservative in a statistical sense (Clauset et al., 2009). We
 197 therefore prefer $M_c=0.9$, a more conservative value for the magnitude of completeness to show
 198 the stability of our further analysis (see text S1 for more details). Our catalog presents a decrease
 199 in the magnitude of completeness in comparison with Vuan et al. (2018), which catalog exhibits a
 200 $M_c=1.8$ considering the same estimation described above.



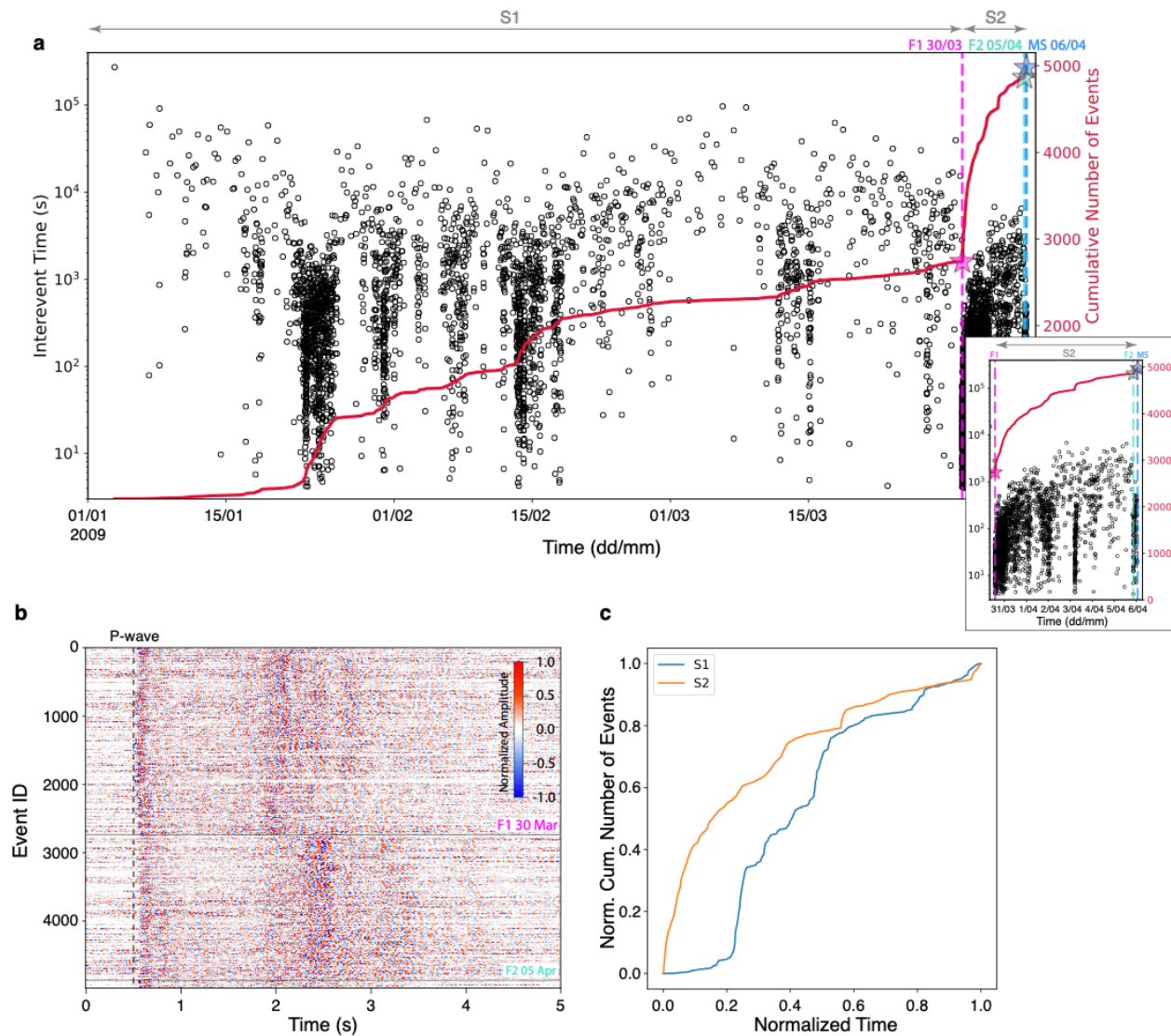
201
 202 **Figure 2:** (a) Magnitude-frequency distribution (0.1 bin) for events detected. (b) Estimated magnitudes (see “Extending Seismic
 203 Catalog” section for more details).

204 This new catalog is the largest catalog for this precursory sequence up to date (Sugan et al.,
 205 2014 has reported 3571 events and Vuan et al., 2018 extended using one station up to 3786 events),

206 and is created using many constrains to ensure high quality of the detections, such as the selection
207 of the templates based on the SNR criteria for P and S waves, higher frequency band, N-value
208 threshold selection using non-physical acausal templates, the relocation to measure the distance
209 between templates and detections, and a longer period of time scanned.

210 Figure 3a shows that the seismicity starts on the 3 January and lasts until the 6 April when
211 the mainshock occurs on the main fault. No seismicity is detected in the period between 6 October
212 2008 to 2 January 2009, so we consider the seismicity starting on the 3 of January as foreshocks
213 of the 9 of April Mw 6.3 earthquake (Chiaraluce et al., 2011; Valoroso et al., 2013; Sugan et al.,
214 2014; Vuan et al., 2018). We observe that the rate of events strongly increases after the occurrence
215 of a Mw 3.9 foreshock on 30 March (F1), which is activating an antithetic fault (Chiaraluce et
216 al., 2011; Valoroso et al., 2013). This activation of the seismicity on the antithetic fault is
217 evidenced in Fig. 3b, which shows a summary of the vertical normalized waveforms for the AQU
218 station (the closest one to the mainshock epicenter, see Fig. 1) aligned on the P-wave arrival. A
219 significant difference of the S-wave arrivals is observed after F1, at the same time as the spatial
220 evolution reported by Chiaraluce et al. (2011) and Valoroso et al. (2013) (see also movie S1). As
221 a first analysis, we split the seismicity before and after F1 on 30 March into two sequences
222 (hereafter S1 and S2, respectively). We observe that the respective cumulative event counts (Fig.
223 3a and c) of sequences S1 and S2 reveal different time evolutions. The seismicity during S1 is
224 characterized by a slow time evolution, with several accelerations occurring over few days (Fig.
225 2, 3a and c) and without any clear mainshock driving them (Fig. 2b). On the other hand, the
226 cumulative number of events in S2 evolves with a log-like behavior similar to an Omori law (Utsu
227 & Ogata, 1995).

228 In the following parts of this work, we track the spatio-temporal evolution of several
229 parameters that describe the style of the seismicity and provide hints about the physical processes
230 active during the foreshock sequence. The mainshock is excluded from this analysis.



231

232 **Figure 3:** Catalog generated using template matching. (a) Interevent times are plotted using black circles, defined as the elapsed
 233 time between consecutive events. Red line represents the cumulative number of events, and fuchsia, turquoise and blue vertical
 234 lines show the time of F1, F2 and mainshock (MS) events, respectively. Inset: closer look showing the time interval between F1
 235 and the mainshock. (b) Normalized waveforms of the catalog for the vertical component of the AQU station, aligned 0.5 s before
 236 estimated P-wave arrival (black vertical dashed line). Event ID is chronologically ordered (i.e., the vertical axis is time-ordered).
 237 Time of occurrence of F1 and F2 are also indicated with black horizontal lines. (c) Comparison between the normalized cumulative
 238 of events for S1 and S2.

239 3 Analysis

240 We study and discuss the spatio-temporal evolution of the seismicity by tracking the time
 241 development of several parameters that characterize the style of seismicity. The parameters are
 242 estimated using moving windows of 100-events with a 99-events overlap i.e., the first estimate
 243 considers the first 100-events and each subsequent estimate is just shifted by one event in time.
 244 This approach allows us to characterize the general evolution of the sequence rather than just
 245 focusing on specific time periods. At this point, it is necessary to consider potential effects of the
 246 magnitude of completeness and the number of events used in each time window. To that scope,

247 we performed tests considering only events with magnitudes larger than the magnitude of
 248 completeness and assess the effect of varying numbers of events for windows-lengths and
 249 overlaps, to evaluate the stability of the results (see Fig. S7-10). A jack-knife process was also
 250 carried out, removing 20% of the catalog in 100 realizations, to assess the uncertainties for each
 251 parameter (Fig. S7-10). Considering the robustness of the tests mentioned above, we present here
 252 the results for the entire catalog (Figs. 4, 5, 6).

253 254 **3.1 Temporal Clustering**

255
 256 Temporal clustering of seismicity, i.e., how past events affect the occurrence of the future
 257 ones, is a key feature of seismicity, and is thought to be principally related to static or dynamic
 258 stress transfer (Freed, 2005). Therefore, the study of temporal clustering probes the degree to
 259 which earthquakes interactions drive the propagation of seismic sequences over external forcing
 260 or other physical processes (Schoenball & Ellsworth, 2017).

261 To quantify the level of time clustering of the seismicity, we estimate the coefficient of
 262 variation (COV) of the interevent times (τ) plotted in Fig. 2a, as $COV(\tau) = \sigma_\tau/\tau$, where σ_τ is the
 263 standard deviation and τ is the average of the interevent times within the window (Kagan &
 264 Jackson, 1990). The COV is 0 for a periodic occurrence of seismicity, 1 for completely random
 265 Poisson occurrence, and larger than 1 for temporally clustered earthquakes; put plainly, the larger
 266 the COV is, the stronger the time clustering is (Kagan & Jackson, 1990; Schoenball & Ellsworth,
 267 2017; Sánchez-Reyes et al., 2021).

268 Fig. 4a shows the temporal evolution of the COV. During S1 we see slow oscillations of
 269 the COV, with generally low values (ranging from 1 to 2.5). We observe that decreases of the
 270 COV are often associated with accelerations of seismicity (Fig. 3a). The lowest values (COV~1)
 271 for S1, are observed during an increase of the seismicity rate starting on 21 January (light cyan
 272 dots in Fig. 4a) and another increase occurring on ~15 February. This observation suggests that
 273 the increment of seismicity rate is not due to interevent stress triggering (e.g., seismicity is not
 274 driven by a mainshock), and an external mechanism should act to increase the number of events
 275 (Beaucé et al., 2019). On the other hand, periods with increased seismicity rates within S2 exhibit
 276 strong, punctual temporal clustering followed by random seismicity akin to mainshock-aftershock
 277 sequences (Schoenball & Ellsworth, 2017). The general evolution of the COV reflects an evolution
 278 of the seismicity style as a function of time, and in particular a clear change of time clustering
 279 when moving from S1 to S2.

280 281 **3.2 Evolution of Seismic Moment Release**

282
 283 The time evolution of the seismic moment (Mo) release reflects the behavior of different
 284 types of seismic sequences and offers insights about the processes on activated faults (Vidale &
 285 Shearer, 2006). While a stable and gradual moment release by many earthquakes without a
 286 dominant large magnitude event is observed for swarm-type sequences (Vidale & Shearer, 2006),
 287 most of the moment is released at once during mainshock-aftershocks sequences (Mogi, 1963).

288 To analyze the time evolution of the seismic moment release, we estimate for each 100-
 289 event sliding window the ratio of the maximum seismic moment to the cumulative seismic moment
 290 ($MaxMo/\sum Mo$, see Fig. 4b). Values close to 1 are related to windows where the largest event
 291 represents most of the Mo released, whereas values close to 0 is observed for windows without a

292 dominant event in terms of moment release. We estimate the moment for each event using the
 293 definition of M_w of Kanamori (1977).

294 Our analysis shows a smooth evolution of the moment ratio during S1 (Fig. 4b), with values
 295 ranging from 0.1 to 0.6. This implies that the seismic moment is released nearly uniformly within
 296 the window, rather than impulsively by some dominant event. From the beginning of the sequence
 297 until the 15 February, the moment ratio is generally low, despite during some periods with
 298 increased seismicity rates when larger events occur (Fig. 4b). From 15 February until F1 we
 299 observe an increase of the moment ratio associated to the occurrence of larger events M2.7 and M
 300 2.9 (17 February and 11 March, respectively. See Fig. 2a and 4b). During S2, the evolution of
 301 moment release is more discontinuous, with large rapid releases of moment, mainly associated
 302 with the occurrence of the largest foreshocks (e.g., F1 and F2). A comparison of Figs. 4a and 4b,
 303 reveals that the coefficient of variation and seismic moment release have similar patterns,
 304 especially during S2, with peak values associated with the occurrence of the largest foreshocks
 305 followed by a rapid decrease of COV and moment release. It is important to note that for the
 306 moment ratio, the size of the selected window has an effect on the observed level of smoothing.
 307 i.e., smaller windows enhance the detection of smaller mainshock-aftershocks sequences (e.g., Fig.
 308 S9), which makes its behavior more episodic and less smooth; this effect is diminished for larger
 309 windows (e.g., Fig. S10).

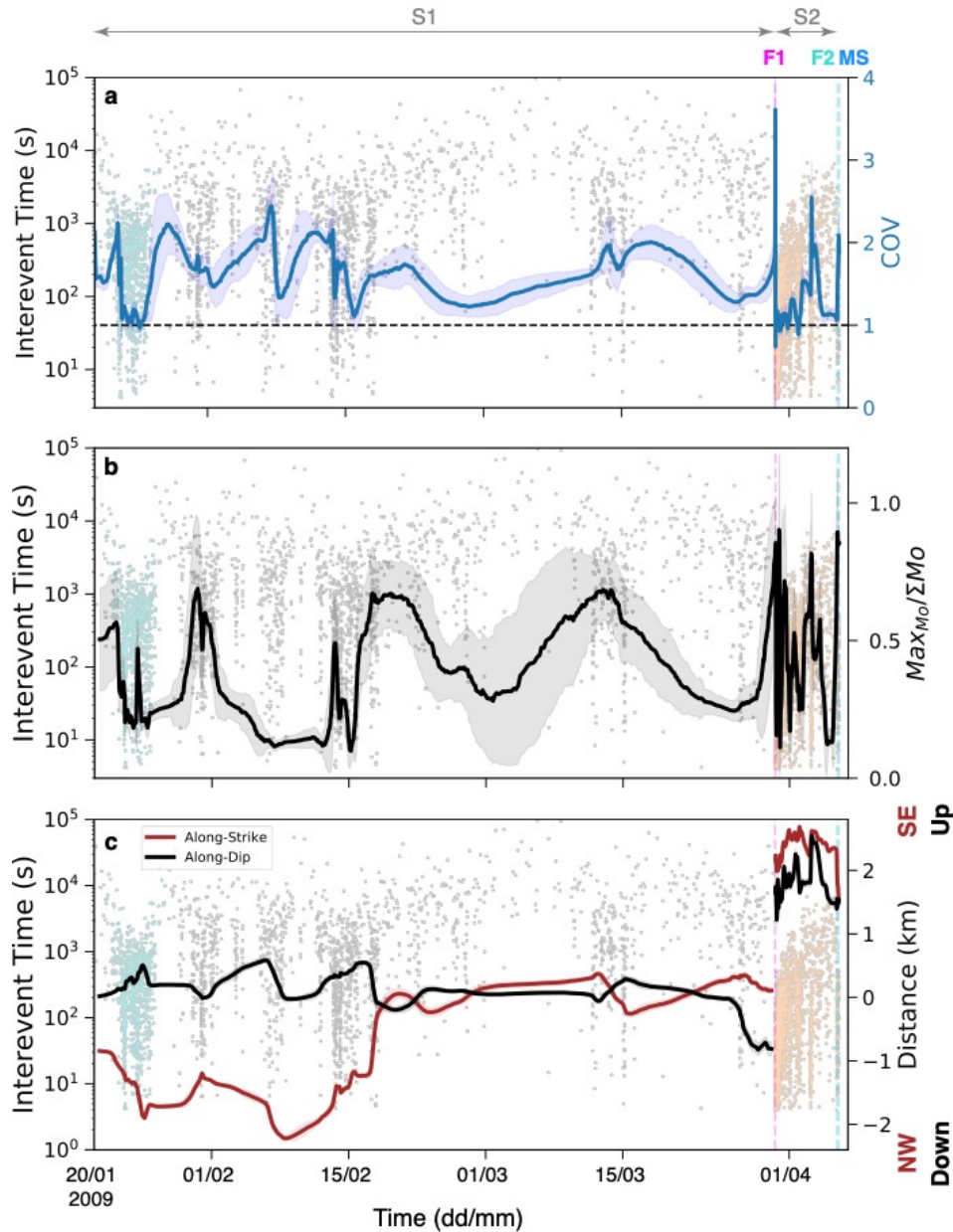
311 3.3 Spatial Evolution

312
 313 To assess the spatial evolution of the seismicity as function of time we track the along-
 314 strike and along-dip position of the events. We first project all the seismicity onto the main fault
 315 plane for S1 (strike N133°E and Dip 50° according to Valoroso et al., 2013) and an orthogonal
 316 fault plane for S2 (where the antithetic fault is active), obtaining along-strike and along-dip
 317 distances measured from the position of the mainshock. We thus track the position of the seismicity
 318 centroid (estimated as the average of all event locations) for each time window, and extract the
 319 along-strike and along-dip coordinates, which are plotted in Fig. 4c. In addition, the 3D evolution
 320 is presented in the supplementary material (see Movie S1).

321 As previously observed by Sukan et al. (2014), the seismicity starts on the north-west
 322 segment of the fault (Fig. 4c). In that region, some slow but significant movement of the centroid
 323 along strike and dip are observed, mainly during increases of the seismicity rate until the 13
 324 February. From such observations along with the 3D spatial evolution presented in Movie S1,
 325 seismicity appears to be re-rupturing the same fault segment. After the initial activity in the NW
 326 segment of the fault, a prominent along-strike migration occurs towards the south-east, observed
 327 in Movie S1 and also tracked by the large along-strike variation of the centroid (Fig. 4c). This
 328 migration begins around 13 February, accelerates on 17 February covering ~1.2 km in less than
 329 24 hours, and fades on 18 February. At this point, the along-dip and along-strike position of the
 330 seismicity stabilize until the end of S1. As an example of the migratory behavior of the seismicity
 331 during S1, the event migration starting on 21 January (group of turquoise dots in Fig. 4) is shown
 332 in Fig. 5a, where velocities on the order of kilometers per day are required to reproduce the
 333 seismicity front (we discuss more details in section 4).

334 During S2 the antithetic fault is activated after the occurrence of F1, and Fig. 4c shows that
 335 the centroid of the seismicity is confined between 1.5 and 2.5 km from the hypocenter both along
 336 dip and strike. In addition, the 3D evolution of the seismicity during S2 (Movie S1) does not exhibit
 337 slow migrations as observed in S1, but rather a rapid spread of the seismicity on the antithetic fault.

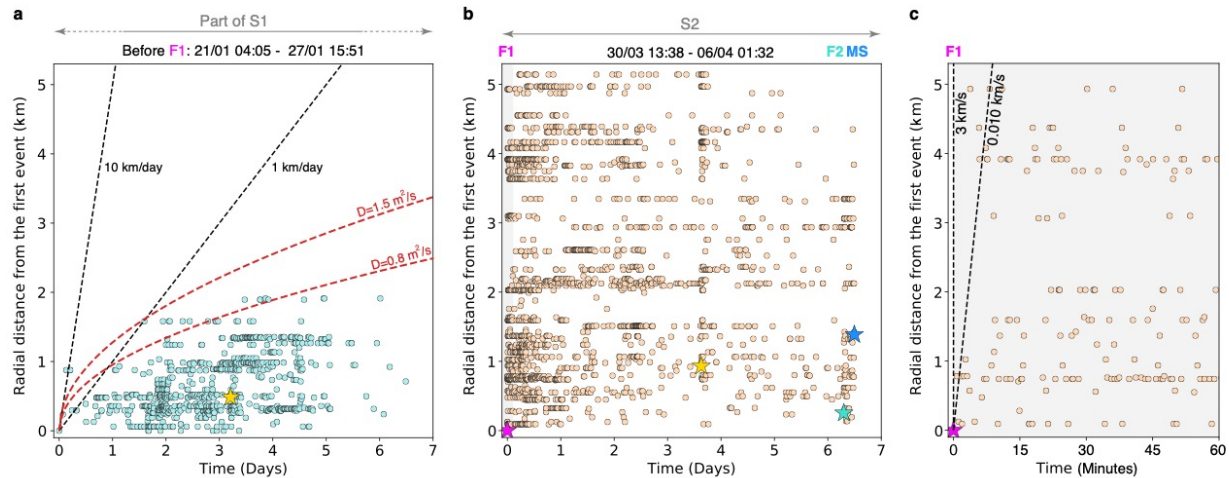
338 This latter behavior is exemplified by Fig. 5b-c, with longer distances (kilometers) rapidly covered
 339 in seconds by seismicity after the occurrence of major events (e.g., F1, F2, and another event
 340 magnitude 3.2 in the middle of the sequence indicated by a yellow star). These distances are longer
 341 than the expected rupture length of M3.9 earthquakes which are about ~400-800 m (e.g., Udias et
 342 al., 2014; Dascher-Cousineau et al., 2020). The strong clustering that we observe from the COV
 343 (Fig. 4a) at the occurrence of large foreshocks in S2 (as F1) together with the rapid large scale
 344 spreading of the seismicity (Vel.=3 km/s), suggest that stress triggering is the main mechanism
 345 driving the seismicity during these bursts (Freed, 2005).



346

347 **Figure 4:** Parameters temporal evolution with a sliding 100-event window length with a 99-event overlap for: (a) Coefficient of
 348 variation of the interevent times (b) Ratio between the maximum value of M_o and its total amount within the window (c) Average
 349 along-strike and along-dip location of the seismicity measured relative to the mainshock (MS) and projected on the main fault.

350 Time corresponds to the time of the last event within the 100-event window (see text). Interevent times plotted in Fig. 3a are also
 351 indicated in Figs. a, b and c (grey dots). Fuchsia, turquoise, and blue vertical dashed lines show the time of F1, F2, and MS events,
 352 respectively. Turquoise and light orange dots represent zoom in presented in Fig. 5.



353 **Figure 5:** (a) Example of radial distance distribution (measured from the first event of the sequence) for a burst during S1 (see Fig.
 354 4). Yellow star represents the largest event within the sequence (M2.4 according to Chiaraluce et al., 2011). Red dashed lines
 355 represent fitted fluid diffusion law (Shapiro et al., 1997) for hydraulic diffusivity of $1.5 \text{ m}^2/\text{s}$ (all the seismicity in a) and $0.8 \text{ m}^2/\text{s}$
 356 (95-percentile of the seismicity in a). (b) Example of radial distance distribution for S2 (see Fig. 4). Fuchsia, turquoise, and blue
 357 vertical stars show the time of F1, F2, and MS events, respectively, and yellow star represent another event magnitude 3.2 in the
 358 middle of the sequence. (c) Zoom for the first 60 minutes plotted in (b).
 359

360

361

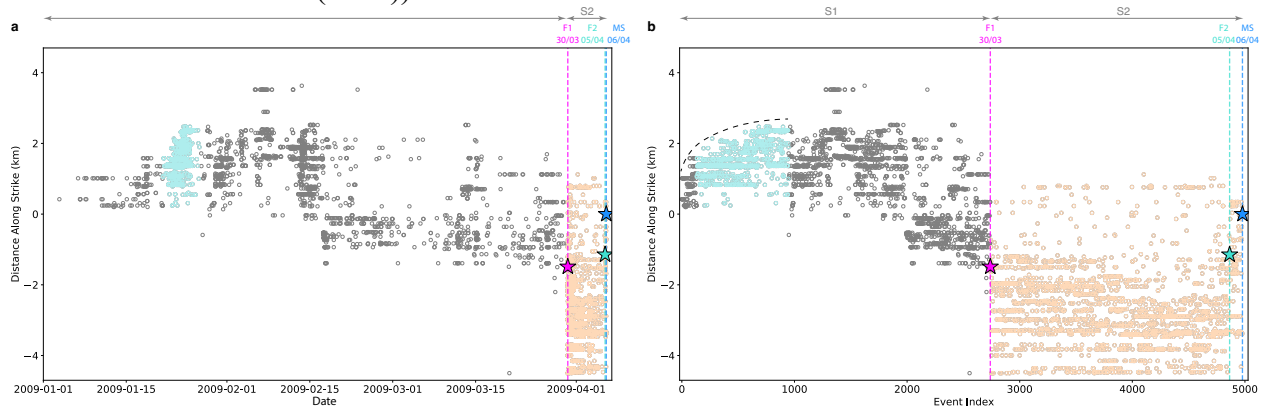
3.4 Event Index evolution of the Sequence

362

363 The migration style of earthquake locations is generally considered to be an important
 364 characteristic to distinguish earthquake swarms from aftershock sequences (Fischer and Hainzl,
 365 2021). While swarms typically show hypocenter migration that depends on the mechanism driving
 366 the swarm (e.g., pore-pressure diffusion (Shapiro et al., 1997), hydraulic fracture growth (Dahm
 367 et al., 2010), or slow slip (Schwartz and Rokosky, 2007)), aftershocks usually occur immediately
 368 across the entire fault plane and along the edges of the mainshock rupture due to stress transfer
 369 (e.g., Freed, 2005) although some longer migrations can be linked to afterslip (e.g., Perfettini et
 370 al., 2018). Usually, the way to analyze such migration patterns is in the distance-time domain,
 371 where the independent variable is typically the time. However, as shown by Fischer & Hainzl
 372 (2021) a complementary analysis tool is to use the event order (e.g., event index) as the
 373 independent variable, which is also termed natural time (Rundle et al., 2018). While using time as
 374 the independent variable permits to resolve if time controls the seismogenic process, using the
 375 event-index indicates if the seismogenic process itself controls the seismicity i.e., every rupture
 376 opens the way for nucleation of the further rupture (Fischer & Hainzl, 2021). Fischer & Hainzl
 377 (2021) showed that an index-plot migration is linear or square-root for either external processes
 378 such as pore-pressure diffusion, hydraulic fracture, and slow slip, or in case of an internal process,
 379 such as the creation of pore-space during ruptures. In contrast to the random (in space) occurrence
 380 of aftershock hypocenters along the mainshock fault plane.

381 Fig. 6 shows the comparison between the time (Fig. 6a) and the event-index (Fig. 6b) plots
 382 for the along-strike position of the seismicity, centered in the mainshock. We can observe that the
 383 patterns of spreading seismicity are observed during S1 (e.g., Fig. 6 a and b, red dots), indicating
 384 that the active area is increasing due to the occurrence of an external seismicity mechanism. On

385 the other hand, during S2 (Fig. 6 a and b, light orange dots) the event-index plot does not show
 386 any migration even removing the time dependence. Instead, we observe a continuous occurrence
 387 of events likely resulting from stress transfer, for which no migration patterns is expected (Fig. 6b,
 388 Helmstetter & Sornette (2003)).



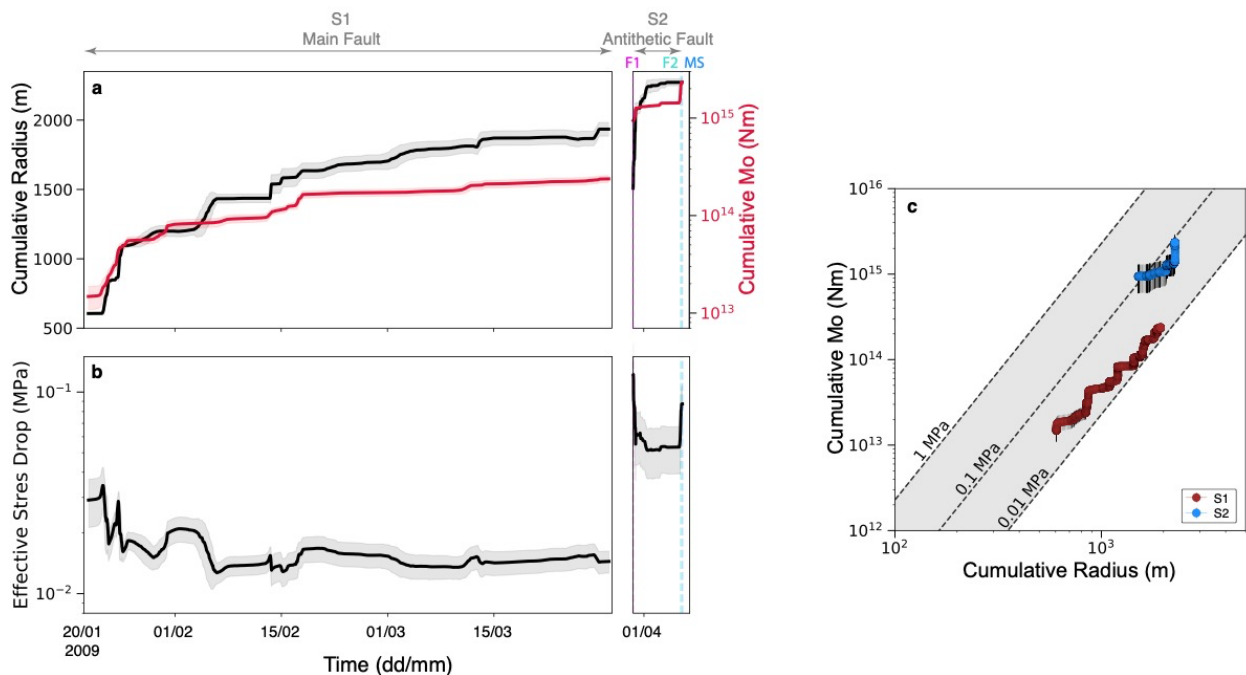
389
 390 **Figure 6:** Along-strike distribution of the seismicity centered in the mainshock for (a) time plot and (b) event-index plot. The
 391 groups of seismicity shown in Fig. 5a are highlighted in turquoise (part of S1) and light orange (S2). Fuchsia, turquoise and blue
 392 vertical lines with stars show the time of F1, F2 and mainshock (MS) events, respectively. Note that the strike considered is the
 393 one of the main fault N133°E (Valoroso et al., 2013).

394 3.5 Effective Stress Drop

395
 396 We further track the temporal evolution of the effective stress drop ($\Delta\sigma_{eff}$) measured by
 397 comparing the cumulative seismic moment and the areal extent of the sequence (Roland &
 398 McGuire, 2009; Fischer & Hainzl, 2017). The region enclosing the seismic events was measured
 399 using a Delaunay triangulation, after projecting all the seismicity onto the main fault plane for S1
 400 (strike N133° and dip 50° according to Valoroso et al., 2013) and an orthogonal fault plane for S2
 401 (where the antithetic fault is active). An example of this process is shown in Fig. S11. Following
 402 Fisher & Hainzl (2017), we impose a distance threshold between neighboring events to avoid
 403 outliers, with a maximum triangle leg length of 2.5 km according to the size of the hypocenter
 404 cloud. As for the previous analysis, the initial window contains 100 events to estimate the rupture
 405 area and the cumulative seismic moment ($\sum M_o$). We then accumulate event by event, and for each
 406 window we derive the effective stress drop as $\Delta\sigma_{eff} = \frac{7}{16} \frac{\sum M_o}{r^3}$ (Fisher & Hainzl, 2017). r is here
 407 the radius of an assumed circle with the same area as estimated from the triangulation. This
 408 procedure was carried out individually for each fault, and their respective results are plotted in Fig.
 409 7.

410 During S1, we observe a rapid increase in both the radius (the region enclosing seismicity)
 411 and the cumulative seismic moment (Fig. 7a) until ~ 25 January. Then, both parameters become
 412 more stable until reaching F1. The first part (S1) of the sequence releases a total seismic moment
 413 of 2.9×10^{14} Nm (\sim Mw 3.6, without considering F1). Different is the behavior of S2, where both
 414 $\sum M_o$ and r rapidly grow, reaching a radius and cumulative seismic moment greater than the values
 415 for S1 in a shorter time. Fig. 7b shows the time evolution of the effective stress drop for both S1
 416 and S2. The comparison between the effective stress drops for S1 and S2 highlights that during
 417 S1, the seismicity take place in an area that is much larger in comparison to the seismic moment
 418 released (Fischer & Hainzl, 2017). This leads to a lower effective stress drops of ~ 0.01 MPa for
 419 S1. Whereas in S2, the higher effective stress drop (~ 0.1 MPa) indicates that most of the area
 420 enclosing the seismicity is seismically active. These values are of the order of effective stress drops

421 estimated by Roland & McGuire (2009) for seismic swarms along Southern California and East
 422 Pacific Rise transform faults. In addition, the difference of almost one order of magnitude between
 423 S1 and S2 is also in concordance with differences in the effective stress drop observed by Fischer
 424 & Hainzl (2017) for different seismic sequences such as injection-induced seismicity, natural
 425 earthquake swarms, and mainshock-aftershock sequences. In addition, we analyze the cumulative
 426 radius against cumulative M_o (Fig. 7c). We observe that our measurements are characterized by a
 427 cubic scaling of seismic moment with earthquake cluster radius ($M_o \propto r^3$) but following different
 428 constant stress drop values. Such scaling is predicted in the case of faults models with brittle or
 429 mixed (brittle and ductile) rheology and homogeneous prestress (Fischer & Hainzl, 2017).
 430 Furthermore, the evolution of the cumulative seismic moment release as a function of the cluster
 431 radius and differences in the effective stress drops can be used to discriminate different physical
 432 processes driving a seismic sequence (e.g., Fischer & Hainzl, 2017). We discuss more in details in
 433 the discussion section.



434
 435 **Figure 7:** Cumulated moment, radius, and effective stress drop evolution. We use 100-events windows-length and 99 events
 436 overlapping for: (a) Cumulated radius (black line) and cumulated moment (red line). (b) Effective stress drop. Time corresponds
 437 to the time of the last event within the 100-events window (see text). (c) Scaling between cumulated radius and cumulated moment
 438 for the first part of the sequence (S1, red dots) and the second part (S2, blue dots).

439 4 Discussions

440 The analysis of the seismicity preceding the Mw 6.3 L'Aquila earthquake reveals a sudden
 441 increase of earthquake activity ~ 3 months prior to the mainshock, in January 2009 (Fig. 2a). From
 442 the beginning of the seismicity to the mainshock, almost 5000 foreshocks released a seismic
 443 moment of $\sim 3 \times 10^{15}$ Nm (\sim Mw 4.3, Fig. 7a). Based on our estimated parameters (Section 3) we
 444 observe that the foreshocks sequence develops in two distinct phases and features a complex
 445 spatio-temporal evolution. The two stages behavior that we report (mostly aseismic, S1, then
 446 mostly seismic, S2) was observed in several other studies, in different tectonic settings (e.g., Kato
 447 et al., 2012; Ruiz et al., 2014, 2017; Socquet et al., 2017; Durand et al., 2020).

448 The first part of the sequence (S1) is characterized by a relatively low temporal interaction
 449 of the seismicity (Fig. 4a), smooth moment release (Fig. 4b) and a slow but significant movement

450 of the centroid of the seismicity (Fig. 4c). We also observe migrations lasting up to 7 days (Fig. 5a
 451 and Fig. 6). The linear velocity of these migrations ranges from 1-10 km/day (Fig. 5a); these
 452 velocities are similar to those associated with seismic swarms driven by aseismic slip (e.g., De
 453 Barros et al., 2020). Finally, we observe migrations in time-space and event-index-space (Fig. 6),
 454 which is indicative that an external seismogenic process controls the seismicity (Fischer and
 455 Hainzl, 2021).

456 If seismicity is a byproduct of aseismic slip, its intermittent time evolution (Fig. 3A)
 457 reflects a variable rate of aseismic slip during the first part of the sequence. A similar behavior is
 458 observed during slow slips in subductions zones, with bursts of aseismic slips mainly occurring in
 459 rapid episodes associated with bursts of tremors and/or low frequency earthquakes (e.g., Rousset
 460 et al., 2019; Jolivet & Frank, 2020). However, confirming the occurrence of aseismic slip using
 461 independent data as GNSS is difficult, as the expected surface displacement expected during the
 462 bursts of seismicity is smaller than the environmental signals often observed in GNSS data along
 463 the Apennines (Amoruso et al., 2017).

464 The observed migrations (Fig. 5a) may also be explained by fluid diffusion (Shapiro et al.,
 465 1997; e.g., Ruhl et al., 2016), considering hydraulic diffusivities of 0.8 and 1.5 m²/s, which are
 466 within expected values for the crust (Scholz, 2019; Talwani & Acree, 1985). If this was the case,
 467 it would be in agreement with the significant role of fluids reported in the region by several authors
 468 (e.g., Antonioli et al., 2005; Lucente et al., 2010; Savage, 2010; Terakawa et al., 2010; Poli et al.,
 469 2020).

470 The second part of the sequence (S2) starts with a magnitude 3.9 event (F1) on the 30 of
 471 April 2009, activating an antithetic fault (Chiaraluce et al., 2011; Valoroso et al., 2013) similarly
 472 to other recent normal fault earthquakes in the region (e.g., Sánchez-Reyes et al., 2021). The
 473 activation of several faults highlights that the precursory process for this event is a complex
 474 volumetric process (Savage et al., 2017; Ben-Zion & Zaliapin, 2020), and is not limited to the fault
 475 plane.

476 S2 is characterized by a high temporal clustering (Fig. 4a) and large moment release (Fig.
 477 4b). These parameters suggest a strong interaction between seismic events, likely governed by
 478 stress triggering (Freed, 2005). No migration is inferred from the event-index analysis (Fig. 6),
 479 and the speed at which seismicity spreads in time is completely different from that observed during
 480 S1. Figs. 5b, c show that after the occurrence of F1, the seismicity covers distances of kilometers
 481 in seconds to minutes, and similar patterns are observed after the occurrence of another magnitude
 482 3.2 event in the middle of S2 (yellow star in Fig. 5b) and after F2. These velocities are not
 483 compatible with mechanisms such as fluid diffusion or aseismic slip, but rather are likely governed
 484 by static or dynamic stress transfer (Freed, 2005).

485 The respective effective stress drops estimated for S1 and S2 are on the order of 0.01 and
 486 0.1 MPa (Fig. 7b). These values are in agreement with estimations in other seismotectonic contexts
 487 (e.g., Roland & McGuire, 2009; Fischer & Hainzl, 2017; Schoenball & Ellsworth, 2017), and the
 488 difference of $\Delta\sigma_{eff}$ between S1 and S2 (Fig. 7b) provide new insights about the physical
 489 mechanisms that might take place during the precursory phase of the studied earthquake. Fischer
 490 & Hainzl (2017) estimated the effective stress drops for several seismic sequences to be in a range
 491 from 8×10^{-5} to 3 MPa. They showed that some sequences such as hydraulic stimulations of
 492 geothermal reservoirs, seismic swarms and mainshock–aftershock-type are associated with
 493 effective stress drops from 0.1 to 3.0 MPa, while smaller values (from 8×10^{-5} to 0.018 MPa)
 494 correspond to sequences that points to a dominating aseismic deformation (e.g., hydraulic
 495 fracturing). Considering the above classification, the low effective stress drop (~ 0.01 MPa) of S1

496 (Fig. 7b) suggests a dominant role of aseismic deformation during the first part of the sequence,
 497 with seismicity occurring over a large area with only a small fraction of the area occupied by
 498 asperities releasing seismic energy. In this model, aseismic slip is the main mechanism triggering
 499 the activation of distant asperities (Fischer & Hainzl, 2017). Following the models proposed by
 500 Fischer & Hainzl (2017) we define S1 as ‘mixed’ model, as it implies a significant ductile region
 501 of the fault with low asperity density. On the other hand, the larger effective stress drop up to ~0.1
 502 MPa after F1 (Fig. 7b) indicates that most of the area enclosing the seismicity is seismically active.
 503 In this case the proximity of asperities favors the stress triggering as mechanism for time clustering
 504 of events (Fig. 4a) over short time scales (Fig. 5b-c). Given these properties, we call this second
 505 model ‘brittle’.

506 Both S1 and S2 show a similar cumulative moment versus radius scaling ($M_o \propto r^3$). This
 507 scaling is observed either in the case of brittle fault rheology or in the mixed fault rheology models
 508 with homogeneous prestress, but with the different stress drop values discussed above (Fischer &
 509 Hainzl, 2017). However, in the case of a partly ductile fault with heterogeneous prestress, the
 510 seismic moment only scales with the square of the radius $M_o \propto r^2$, which is not consistent with
 511 our observations (Fischer & Hainzl, 2017, Fig. 7c). Considering that the mixed model is
 512 representative of S1, and the brittle model of S2 due to the variations of the effective stress drop
 513 (Fig. 7c), we discuss possible differences between the fault rheologies in S1 and S2.

514 In the case of brittle asperities embedded in a ductile environment (mixed model during
 515 S1), numerical simulations indicate that two scenarios might occur. Either the asperities rupture
 516 simultaneously as a single earthquake or separately as individual events, depending on the distance
 517 between the asperities and the frictional strength of the ductile region (Kaneko et al., 2010;
 518 Dublanche et al., 2013; Yabe and Ide, 2017). Thus, high density of the asperities and/or a small
 519 $a - b$ frictional parameter in the ductile region lead to simultaneous rupturing of the asperities,
 520 while a lower asperity density leads to isolated ruptures, producing a sequence of ruptures with
 521 diminished time interaction between each other (Kaneko et al., 2010; Dublanche et al., 2013; Yabe
 522 and Ide, 2017). During S1, the low effective stress drop (Fig. 7b) is resulting from void fault areas
 523 deformed aseismically among adjacent ruptures, which did not contribute to the seismic moment
 524 release (Fischer & Hainzl, 2017, 2021). In this scenario, the existence of large inter-asperities
 525 distances is also consistent with the low seismicity interactions inferred from the COV values (Fig.
 526 4a)

527 For the case of a brittle fault rheology (S2), the fault segment consists of densely distributed
 528 asperities that can rupture individually (Fischer & Hainzl, 2017). For this, some mechanism that
 529 prevents the simultaneous rupture of the entire segment and leads to a piecewise rupturing of the
 530 fault segment by numerous small earthquakes is needed. Following Yamashita (1999) and Aki and
 531 Richards (2002), possible mechanisms might be the presence of barriers, inhomogeneous loading,
 532 or dilatancy due to pore creation, a process suggested by Lucente et al., (2010) after the occurrence
 533 of F1. In this model, due to the proximity between asperities, the elastic stress plays an important
 534 role during the rupture process. This corresponds closely to what our observations indicate during
 535 S2: larger COV values (Fig. 4a), episodic and rapid releases of the seismic moment (Fig. 4b) and
 536 seismicity covering larger distances of kilometers in short time from seconds to minutes (Fig. 5b,
 537 c).

538 The observed cubic scaling between the accumulated seismic moment and radius is also
 539 indicative of re-rupturing for the two models mentioned above (Fischer & Hainzl, 2017). The re-
 540 rupturing implies significant overlap between regions hosting subsequent seismic events. This

541 behavior is observed during S1, as reactivation of earthquake families during multiple
542 accelerations of seismicity (Fig. 4c, Movie S1, Fig. S12).

543 The models of Fischer & Hainzl (2017) suggest that the rerupturing process is expected to
544 continue until the stress is fully released within the whole fault segment. Interestingly, although
545 the seismicity of S1 occurs on the fault plane that slipped during the mainshock (Chiaraluce et al.,
546 2011), there is no overlap between the coseismic slip and the foreshocks (Valoroso et al., 2013,
547 Fig. S13). This suggest that this part of the fault released the full stress in an intermittent fashion
548 through foreshocks (Fig. 4b), as the localized fault properties prohibit the nucleation of a large slip
549 episode. Similar behavior has been observed in modeling, where small events appear at the
550 transition from the locked to creeping behavior toward the bottom of the seismogenic zone with
551 decreasing values of the characteristic slip distance of the friction law (Lapusta & Rice, 2003).
552

553 **5 Conclusion**

554
555 The analysis of our high-resolution seismic catalog highlights a number of different
556 physical mechanisms that played a role during the precursory phase of the L'Aquila earthquake.
557 Our results also demonstrate how the faults involved in the sequence present quantitative
558 differences in the earthquake activity they host. While the seismicity occurring on the main fault
559 up to one week before the mainshock (S1) exhibits small time clustering, smooth moment release,
560 slow migrations and a lower effective stress drop, the seismicity occurring on the antithetic fault
561 after F1 (S2) shows strong punctual clustering and moment release, a rapid spreading of the
562 seismicity and larger effective stress drop. Such differences in the seismicity behavior indicate that
563 while an external process (aseismic or fluid diffusion, or likely a combination of both) is driving
564 the seismicity in S1, stress transfer is the dominant mechanism during S2. A comparison of our
565 observations with recent seismic swarm models (Fischer and Hainzl, 2017) indicates that during
566 S1 a mixed rheology model of brittle asperities embedded in a ductile environment and large inter-
567 asperity distances is likely. On the other hand, a brittle fault rheology with a dense population of
568 asperities and small inter-asperity distances is more plausible for the antithetic fault during S2.

569 Our study shows a complex coalescence of different physical processes occurring during
570 the precursory phase of a large earthquake. Moreover, we highlight how the quantitative analysis
571 of spatio-temporal evolution of microseismicity, can unveil complex precursory behaviors, which
572 differ from nucleation models based on simple planar faults models (Dieterich, 1992; Marone,
573 1998; Liu & Rice, 2005; Rubin & Ampuero, 2005) aiming for more complex scenarios (e.g., Zhang
574 et al., 2014; Dutta et al., 2021, Shimizu et al., 2021).
575

576 **Data Availability**

577 Data was downloaded from the Istituto Nazionale di Geofisica e Vulcanologia (INGV, 2006)
578 using obspyDMT (<https://github.com/kasra-hosseini/obsypyDMT>, Hosseini and Sigloch, 2017).
579 The fast matched filter (Beaucé et al., 2018) used in this study can be found at
580 https://github.com/beridel/fast_matched_filter. Computations were performed using the
581 University of Grenoble Alpes (UGA) High-Performance Computing infrastructures CIMENT
582 (https://ciment.univ-grenoble-alpes.fr/wiki-pub/index.php/Welcome_to_the_CIMENT_site!).

583 The catalog generated here is available at <https://doi.org/10.5281/zenodo.4776701> (last accessed
584 20 May 2021).

585 **Acknowledgments**

586 LC and PP were supported by the European Union Horizon 2020 Research and Innovation
587 Programme (grant agreements, 802777-MONIFaults). WBF was supported by the National
588 Science Foundation grant EAR-2103408. LC and WBF were also supported by the Thomas
589 Jefferson Fund award #093

590 **References**

- 591
592 Acosta, M., Passelègue, F. X., Schubnel, A., Madariaga, R., & Violay, M. (2019). Can precursory
593 moment release scale with earthquake magnitude? A view from the laboratory. *Geophysical*
594 *Research Letters*, *46*(22), 12927-12937.
595
- 596 Aki, K., and P. G. Richards (2002). *Quantitative Seismology*, Second Ed., University Science
597 Books, Sausalito, California, 574.
598
- 599 Amoruso, A., Crescentini, L., & Chiaraluce, L. (2017). Surface temperature and precipitation
600 affecting GPS signals before the 2009 L'Aquila earthquake (Central Italy). *Geophysical Journal*
601 *International*, *210*(2), 911-918.
602
- 603 Antonioli, A., Piccinini, D., Chiaraluce, L., & Cocco, M. (2005). Fluid flow and seismicity pattern:
604 Evidence from the 1997 Umbria-Marche (central Italy) seismic sequence. *Geophysical Research*
605 *Letters*, *32*(10).
606
- 607 Beaucé, E., Frank, W. B., & Romanenko, A. (2018). Fast matched filter (FMF): An efficient
608 seismic matched-filter search for both CPU and GPU architectures. *Seismological Research*
609 *Letters*, *89*(1), 165-172.
610
- 611 Beaucé, E., Frank, W. B., Paul, A., Campillo, M., & van der Hilst, R. D. (2019). Systematic
612 detection of clustered seismicity beneath the Southwestern Alps. *Journal of Geophysical*
613 *Research: Solid Earth*, *124*(11), 11531-11548.
614
- 615 Ben-Zion, Y., & Zaliapin, I. (2020). Localization and coalescence of seismicity before large
616 earthquakes. *Geophysical Journal International*, *223*(1), 561-583.
617
- 618 Boncio, P., Pizzi, A., Brozzetti, F., Pomposo, G., Lavecchia, G., Di Naccio, D., & Ferrarini, F.
619 (2010). Coseismic ground deformation of the 6 April 2009 L'Aquila earthquake (central Italy,
620 Mw6.3). *Geophysical Research Letters*, *37*(6).
621
- 622 Bouchon, M., Karabulut, H., Aktar, M., Özalaybey, S., Schmittbuhl, J., & Bouin, M. P. (2011).
623 Extended nucleation of the 1999 Mw 7.6 Izmit earthquake. *Science*, *331*(6019), 877-880.
624
- 625 Bouchon, M., Durand, V., Marsan, D., Karabulut, H., & Schmittbuhl, J. (2013). The long
626 precursory phase of most large interplate earthquakes. *Nature geoscience*, *6*(4), 299-302.
627
- 628 Cabrera, L., Ruiz, S., Poli, P., Contreras-Reyes, E., Osses, A., & Mancini, R. (2020). Northern
629 Chile intermediate-depth earthquakes controlled by plate hydration. *Geophysical Journal*
630 *International*.
631
- 632 Chen, X., & Shearer, P. M. (2013). California foreshock sequences suggest aseismic triggering
633 process. *Geophysical Research Letters*, *40*(11), 2602-2607.
634

- 635 Cheloni, D., D'agostino, N., D'anastasio, E., Avallone, A., Mantenuto, S., Giuliani, R., Mattone,
636 M., Calcaterra, S., Gambino, P., Dominici, D., Radicioni, F. & Fastellini, G. (2010). Coseismic
637 and initial post-seismic slip of the 2009 M w 6.3 L'Aquila earthquake, Italy, from GPS
638 measurements. *Geophysical Journal International*, 181(3), 1539-1546.
639
- 640 Chiaraluce, L., Valoroso, L., Piccinini, D., Di Stefano, R., & De Gori, P. (2011). The anatomy of
641 the 2009 L'Aquila normal fault system (central Italy) imaged by high resolution foreshock and
642 aftershock locations. *Journal of Geophysical Research: Solid Earth*, 116(B12).
643
- 644 Cirella, A., Piatanesi, A., Cocco, M., Tinti, E., Scognamiglio, L., Michelini, A., Lomax, A. &
645 Boschi, E. (2009). Rupture history of the 2009 L'Aquila (Italy) earthquake from non-linear joint
646 inversion of strong motion and GPS data. *Geophysical Research Letters*, 36(19).
647
- 648 Cirella, A., Piatanesi, A., Tinti, E., Chini, M., & Cocco, M. (2012). Complexity of the rupture
649 process during the 2009 L'Aquila, Italy, earthquake. *Geophysical Journal International*, 190(1),
650 607-621.
651
- 652 Clauset, A., Shalizi, C. R., & Newman, M. E. (2009). Power-law distributions in empirical data.
653 *SIAM review*, 51(4), 661-703.
654
- 655 Dahm, T., Hainzl, S., and Fischer, T. (2010). Bidirectional and unidirectional fracture growth
656 during hydrofracturing: role of driving stress gradients. *J. Geophys. Res.* 115, B12322.
657 doi:10.1029/2009jb006817.
658
- 659 Dascher-Cousineau, K., Brodsky, E. E., Lay, T., & Goebel, T. H. (2020). What controls variations
660 in aftershock productivity?. *Journal of Geophysical Research: Solid Earth*, 125(2),
661 e2019JB018111.
662
- 663 De Barros, L., Cappa, F., Deschamps, A., & Dublanchet, P. (2020). Imbricated aseismic slip and
664 fluid diffusion drive a seismic swarm in the Corinth Gulf, Greece. *Geophysical Research Letters*,
665 47(9), e2020GL087142.
666
- 667 Dieterich, J. H. (1992). Earthquake nucleation on faults with rate-and state-dependent
668 strength. *Tectonophysics*, 211(1-4), 115-134.
669
- 670 Dodge, D. A., Beroza, G. C., & Ellsworth, W. L. (1995). Foreshock sequence of the 1992 Landers,
671 California, earthquake and its implications for earthquake nucleation. *Journal of Geophysical
672 Research: Solid Earth*, 100(B6), 9865-9880.
673
- 674 Dodge, D. A., Beroza, G. C., & Ellsworth, W. L. (1996). Detailed observations of California
675 foreshock sequences: Implications for the earthquake initiation process. *Journal of Geophysical
676 Research: Solid Earth*, 101(B10), 22371-22392.
677
678

- 679 Dublanchet, P., P. Bernard, and P. Favreau (2013). Interactions and triggering in a 3-D rate-and-
680 state asperity model, *Journal of Geophysical Research: Solid Earth* 118, 2225– 2245, doi:
681 10.1002/jgrb.50187.
- 682
- 683 Durand, V., Bentz, S., Kwiatek, G., Dresen, G., Wollin, C., Heidbach, O., Marínez-Garzón, P.,
684 Cotton, F., Nurlu, M. & Bohnhoff, M. (2020). A Two-Scale Preparation Phase Preceded an M w
685 5.8 Earthquake in the Sea of Marmara Offshore Istanbul, Turkey. *Seismological Society of*
686 *America*, 91(6), 3139-3147.
- 687
- 688 Dutta, R., Jónsson, S., & Vasyura-Bathke, H. (2021). Simultaneous Bayesian Estimation of Non-
689 Planar Fault Geometry and Spatially-Variably Slip. *Journal of Geophysical Research: Solid Earth*,
690 e2020JB020441.
- 691
- 692 Ellsworth, W. L., & Beroza, G. C. (1995). Seismic evidence for an earthquake nucleation
693 phase. *Science*, 268(5212), 851-855.
- 694
- 695 Ellsworth, W. L., & Bulut, F. (2018). Nucleation of the 1999 Izmit earthquake by a triggered
696 cascade of foreshocks. *Nature Geoscience*, 11(7), 531-535.
- 697
- 698 Falcucci, E., Gori, S., Peronace, E., Fubelli, G., Moro, M., Saroli, M., Giaccio, B., Messina, P.,
699 Naso, G., Scardia, G., Sposato, A., Voltaggio, M., Galli, P. & Galadini, F. (2009). The Paganica
700 fault and surface coseismic ruptures caused by the 6 April 2009 earthquake (L'Aquila, central
701 Italy). *Seismological Research Letters*, 80(6), 940-950.
- 702
- 703 Fischer, T., & Hainzl, S. (2017). Effective stress drop of earthquake clusters. *Bulletin of the*
704 *Seismological Society of America*, 107(5), 2247-2257.
- 705
- 706 Fischer, T., & Hainzl, S. (2021). The Growth of Earthquake Clusters. *Frontiers in Earth*
707 *Science*, 9, 79.
- 708
- 709 Frank, W. B., Poli, P., & Perfettini, H. (2017). Mapping the rheology of the Central Chile
710 subduction zone with aftershocks. *Geophysical Research Letters*, 44(11), 5374-5382.
- 711
- 712 Gardonio, B., Campillo, M., Marsan, D., Lecointre, A., Bouchon, M., & Letort, J. (2019). Seismic
713 activity preceding the 2011 M w 9.0 Tohoku earthquake, Japan, analyzed with multidimensional
714 template matching. *Journal of Geophysical Research: Solid Earth*, 124(7), 6815-6831.
- 715
- 716 Gibbons, S. J., & Ringdal, F. (2006). The detection of low magnitude seismic events using array-
717 based waveform correlation. *Geophysical Journal International*, 165(1), 149-166.
- 718
- 719 Helmstetter, A., & Sornette, D. (2002). Diffusion of epicenters of earthquake aftershocks, Omori's
720 law, and generalized continuous-time random walk models. *Physical Review E*, 66(6), 061104.
- 721

- 722 Herrmann, M., & Marzocchi, W. (2021). Inconsistencies and lurking pitfalls in the magnitude–
723 frequency distribution of high-resolution earthquake catalogs. *Seismological Society of America*,
724 *92(2A)*, 909-922.
725
- 726 Hosseini, K., and K. Sigloch (2017). Obspydmt: A python toolbox for retrieving and processing
727 large seismological data sets, *Solid Earth* 8, no. 5, 1047–1070.
728
- 729 INGV Seismological Data Centre. (2006, January 1). Rete Sismica Nazionale (RSN). Istituto
730 Nazionale di Geofisica e Vulcanologia (INGV), Italy.
731 <https://doi.org/10.13127/SD/X0FXNH7QFY>.
732
- 733 Jolivet, R., & Frank, W. B. (2020). The transient and intermittent nature of slow slip. *AGU*
734 *Advances*, 1(1), e2019AV000126.
735
- 736 Kagan, Y. Y., & Jackson, D. D. (1991). Long-term earthquake clustering. *Geophysical Journal*
737 *International*, *104(1)*, 117-133.
738
- 739 Kanamori, H., & Anderson, D. L. (1975). Theoretical basis of some empirical relations in
740 seismology. *Bulletin of the seismological society of America*, *65(5)*, 1073-1095.
741
- 742 Kaneko, Y., J.-P. Avouac, and N. Lapusta (2010). Towards inferring earth- quake patterns from
743 geodetic observations of interseismic coupling, *Nature Geoscience* 3, 363–369, doi:
744 10.1038/NNGEO843.
745
- 746 Kato, A., Obara, K., Igarashi, T., Tsuruoka, H., Nakagawa, S., & Hirata, N. (2012). Propagation
747 of slow slip leading up to the 2011 Mw 9.0 Tohoku-Oki earthquake. *Science*, *335(6069)*, 705-708.
748
- 749 Kato, A., & Ben-Zion, Y. (2020). The generation of large earthquakes. *Nature Reviews Earth &*
750 *Environment*, 1-14.
751
- 752 Lapusta, N., & Rice, J. R. (2003). Nucleation and early seismic propagation of small and large
753 events in a crustal earthquake model. *Journal of Geophysical Research: Solid Earth*, *108(B4)*.
754
- 755 Liu, Y., & Rice, J. R. (2005). Aseismic slip transients emerge spontaneously in three-dimensional
756 rate and state modeling of subduction earthquake sequences. *Journal of Geophysical Research:*
757 *Solid Earth*, *110(B8)*.
758
- 759 Marone, C. (1998). The effect of loading rate on static friction and the rate of fault healing during
760 the earthquake cycle. *Nature*, *391(6662)*, 69-72.
761
- 762 MedNet Project Partner Institutions. (1990, January 1). Mediterranean Very Broadband
763 Seismographic Network (MedNet). Istituto Nazionale di Geofisica e Vulcanologia (INGV).
764 <https://doi.org/10.13127/SD/FBBBTDTD6Q>.
765

- 766 Meng, H., & Fan, W. (2021). Immediate foreshocks indicating cascading rupture developments
767 for 527 M 0.9 to 5.4 Ridgecrest earthquakes. *Geophysical Research Letters*, e2021GL095704.
768
- 769 McLaskey, G. C., & Kilgore, B. D. (2013). Foreshocks during the nucleation of stick-slip
770 instability. *Journal of Geophysical Research: Solid Earth*, 118(6), 2982-2997.
771
- 772 McLaskey, G. C., & Lockner, D. A. (2014). Preslip and cascade processes initiating laboratory
773 stick slip. *Journal of Geophysical Research: Solid Earth*, 119(8), 6323-6336.
774
- 775 McLaskey, G. C. (2019). Earthquake initiation from laboratory observations and implications for
776 foreshocks. *Journal of Geophysical Research: Solid Earth*, 124(12), 12882-12904.
777
- 778 Mogi, K. (1963). Some discussions on aftershocks, foreshocks and earthquake swarms: the
779 fracture of a semi-infinite body caused by an inner stress origin and its relation to the earthquake
780 phenomena (third paper). *Bulletin of the Earthquake Research Institute, University of*
781 *Tokyo*, 41(3), 615-658.
782
- 783 Omori, F. (1908). On the Fore-shocks of Earthquakes. *Bulletin of the Imperial Earthquake*
784 *Investigation Committee*, 2(2), 89-100.
785
- 786 Peng, Z., & Zhao, P. (2009). Migration of early aftershocks following the 2004 Parkfield
787 earthquake. *Nature Geoscience*, 2(12), 877-881.
788
- 789 Perfettini, H., Frank, W. B., Marsan, D., & Bouchon, M. (2018). A model of aftershock migration
790 driven by afterslip. *Geophysical Research Letters*, 45(5), 2283-2293.
791
- 792 Poli, P., Marguin, V., Wang, Q., D'agostino, N., & Johnson, P. (2020). Seasonal and Coseismic
793 Velocity Variation in the Region of L'Aquila From Single Station Measurements and Implications
794 for Crustal Rheology. *Journal of Geophysical Research: Solid Earth*, 125(7), e2019JB019316.
795
- 796 Roland, E., & McGuire, J. J. (2009). Earthquake swarms on transform faults. *Geophysical Journal*
797 *International*, 178(3), 1677-1690.
798
- 799 Ross, Z. E., Trugman, D. T., Hauksson, E., & Shearer, P. M. (2019). Searching for hidden
800 earthquakes in Southern California. *Science*, 364(6442), 767-771.
801
- 802 Rubin, A. M., & Ampuero, J. P. (2005). Earthquake nucleation on (aging) rate and state
803 faults. *Journal of Geophysical Research: Solid Earth*, 110(B11).
804
- 805 Ruhl, C. J., Abercrombie, R. E., Smith, K. D., & Zaliapin, I. (2016). Complex spatiotemporal
806 evolution of the 2008 Mw 4.9 Mogul earthquake swarm (Reno, Nevada): Interplay of fluid and
807 faulting. *Journal of Geophysical Research: Solid Earth*, 121(11), 8196-8216.
808
- 809 Ruiz, S., Metois, M., Fuenzalida, A., Ruiz, J., Leyton, F., Grandin, R., Vigny, C., Madariaga, R.
810 & Campos, J. (2014). Intense foreshocks and a slow slip event preceded the 2014 Iquique Mw 8.1
811 earthquake. *Science*, 345(6201), 1165-1169.

812

813 Ruiz, S., Aden-Antoniow, F., Baez, J. C., Otarola, C., Potin, B., Del Campo, F., Poli, P., Flores,
814 C., Satriano, C., Leyton, F., Madariaga, R. & Bernard, P. (2017). Nucleation phase and dynamic
815 inversion of the Mw 6.9 Valparaíso 2017 earthquake in Central Chile. *Geophysical Research*
816 *Letters*, 44(20), 10-290.

817

818 Rundle, J. B., Luginbuhl, M., Giguere, A., and Turcotte, D. L. (2018). Natural time, nowcasting
819 and the physics of earthquakes: estimation of seismic risk to global megacities. *Pure Appl.*
820 *Geophys.* 175, 647–660. doi:10.1007/s00024-017-1720-x.

821

822 Rousset, B., Fu, Y., Bartlow, N., & Bürgmann, R. (2019). Weeks-Long and Years-Long Slow Slip
823 and Tectonic Tremor Episodes on the South Central Alaska Megathrust. *Journal of Geophysical*
824 *Research: Solid Earth*, 124(12), 13392-13403.

825

826 Sánchez-Reyes, H., Essing, D., Beaucé, E., & Poli, P. (2021). The Imbricated Foreshock and
827 Aftershock Activities of the Balsorano (Italy) Mw 4.4 Normal Fault Earthquake and Implications
828 for Earthquake Initiation. *Seismological Society of America*.

829

830 Savage, M. K. (2010). The role of fluids in earthquake generation in the 2009 Mw 6.3 L'Aquila,
831 Italy, earthquake and its foreshocks. *Geology*, 38(11), 1055-1056.

832

833 Savage, H. M., Keranen, K. M., P. Schaff, D., & Dieck, C. (2017). Possible precursory signals in
834 damage zone foreshocks. *Geophysical Research Letters*, 44(11), 5411-5417.

835

836 Scholz, C. H. (2019). *The mechanics of earthquakes and faulting*. Cambridge university press.

837

838 Schoenball, M., & Ellsworth, W. L. (2017). A systematic assessment of the spatiotemporal
839 evolution of fault activation through induced seismicity in Oklahoma and southern
840 Kansas. *Journal of Geophysical Research: Solid Earth*, 122(12), 10-189.

841

842 Schwartz, S. Y., and Rokosky, J. M. (2007). Slow slip events and seismic tremor at circum-pacific
843 subduction zones. *Rev. Geophys.* 45, a. doi:10.1029/2006RG000208

844

845 Scognamiglio, L., Tinti, E., Michelini, A., Dreger, D. S., Cirella, A., Cocco, M., Mazza, S. &
846 Piatanesi, A. (2010). Fast determination of moment tensors and rupture history: What has been
847 learned from the 6 April 2009 L'Aquila earthquake sequence. *Seismological Research*
848 *Letters*, 81(6), 892-906.

849

850 Shapiro, S. A., Huenges, E., & Borm, G. (1997). Estimating the crust permeability from fluid-
851 injection-induced seismic emission at the KTB site. *Geophysical Journal International*, 131(2),
852 F15-F18.

853

- 854 Shelly, D. R. (2020). A high-resolution seismic catalog for the initial 2019 Ridgecrest earthquake
855 sequence: Foreshocks, aftershocks, and faulting complexity. *Seismological Research*
856 *Letters*, 91(4), 1971-1978.
857
- 858 Shimizu, K., Yagi, Y., Okuwaki, R., & Fukahata, Y. (2021). Construction of fault geometry by
859 finite-fault inversion of teleseismic data. *Geophysical Journal International*, 224(2), 1003-1014.
860
- 861 Simon, V., Kraft, T., Diehl, T., & Tormann, T. Possible Precursory Slow-Slip to two ML~ 3
862 Mainevents of the Diemtigen Microearthquake Sequence, Switzerland. *Geophysical Research*
863 *Letters*, e2021GL093783.
864
- 865 Socquet, A., Valdes, J. P., Jara, J., Cotton, F., Walpersdorf, A., Cotte, N., Specht, S., Ortega-
866 Culaciati, F., Carrizo, D., & Norabuena, E. (2017). An 8 month slow slip event triggers
867 progressive nucleation of the 2014 Chile megathrust. *Geophysical Research Letters*, 44(9), 4046-
868 4053.
869
- 870 Sugan, M., Kato, A., Miyake, H., Nakagawa, S., & Vuan, A. (2014). The preparatory phase of the
871 2009 Mw 6.3 L'Aquila earthquake by improving the detection capability of low-magnitude
872 foreshocks. *Geophysical Research Letters*, 41(17), 6137-6144.
873
- 874 Talwani, P., & Acree, S. (1985). Pore pressure diffusion and the mechanism of reservoir-induced
875 seismicity. In *Earthquake prediction* (pp. 947-965). Birkhäuser, Basel.
876
- 877 Tape, C., Holtkamp, S., Silwal, V., Hawthorne, J., Kaneko, Y., Ampuero, J. P., Ji, C., Ruppert, N.,
878 Smith, K., & West, M. E. (2018). Earthquake nucleation and fault slip complexity in the lower
879 crust of central Alaska. *Nature Geoscience*, 11(7), 536-541.
880
- 881 Terakawa, T., Zoporowski, A., Galvan, B., & Miller, S. A. (2010). High-pressure fluid at
882 hypocentral depths in the L'Aquila region inferred from earthquake focal
883 mechanisms. *Geology*, 38(11), 995-998.
884
- 885 Trugman, D. T., & Shearer, P. M. (2017). GrowClust: A hierarchical clustering algorithm for
886 relative earthquake relocation, with application to the Spanish Springs and Sheldon, Nevada,
887 earthquake sequences. *Seismological Research Letters*, 88(2A), 379-391.
888
- 889 Utsu, T., & Ogata, Y. (1995). The centenary of the Omori formula for a decay law of aftershock
890 activity. *Journal of Physics of the Earth*, 43(1), 1-33.
891
- 892 Valoroso, L., Chiaraluce, L., Piccinini, D., Di Stefano, R., Schaff, D., & Waldhauser, F. (2013).
893 Radiography of a normal fault system by 64,000 high-precision earthquake locations: The 2009
894 L'Aquila (central Italy) case study. *Journal of Geophysical Research: Solid Earth*, 118(3), 1156-
895 1176.
896

- 897 Vidale, J. E., & Shearer, P. M. (2006). A survey of 71 earthquake bursts across southern California:
 898 Exploring the role of pore fluid pressure fluctuations and aseismic slip as drivers. *Journal of*
 899 *Geophysical Research: Solid Earth*, *111*(B5).
 900
- 901 Vuan, A., Sukan, M., Amati, G., & Kato, A. (2018). Improving the Detection of Low-Magnitude
 902 Seismicity Preceding the Mw 6.3 L'Aquila Earthquake: Development of a Scalable Code Based
 903 on the Cross Correlation of Template Earthquakes Improving the Detection of Low-Magnitude
 904 Seismicity Preceding the Mw 6.3 L'Aquila Earthquake. *Bulletin of the Seismological Society of*
 905 *America*, *108*(1), 471-480.
 906
- 907 Yabe, S., and S. Ide (2017). Slip-behavior transitions of a heterogeneous linear fault, *Journal of*
 908 *Geophysical Research: Solid Earth* *122*, 387–410, doi: 10.1002/2016JB013132.
 909
- 910 Yamashita, T. (1999). Pore creation due to fault slip in a fluid-permeated fault zone and its effect
 911 on seismicity: Mechanism of earthquake swarm, *Pure Appl. Geophys.* *155*, 625–647.
 912
- 913 Yoon, C. E., Yoshimitsu, N., Ellsworth, W. L., & Beroza, G. C. (2019). Foreshocks and mainshock
 914 nucleation of the 1999 M w 7.1 Hector Mine, California, Earthquake. *Journal of Geophysical*
 915 *Research: Solid Earth*, *124*(2), 1569-1582.
 916
- 917 Zhang, Z., Zhang, W., & Chen, X. (2014). Three-dimensional curved grid finite-difference
 918 modelling for non-planar rupture dynamics. *Geophysical Journal International*, *199*(2), 860-879.
 919

920 **References in Supplementary Material**

- 921
- 922 Cirella, A., Piatanesi, A., Tinti, E., Chini, M., & Cocco, M. (2012). Complexity of the rupture
 923 process during the 2009 L'Aquila, Italy, earthquake. *Geophysical Journal International*, *190*(1),
 924 607-621.
 925
- 926 Clauset, A., C. R. Shalizi, and M. E. J. Newman (2009). Power-law distributions in empirical data,
 927 *SIAM Rev.* *51*, no. 4, 661–703, doi: 10.1137/070710111.
 928
- 929 De Gori, P., Lucente, F. P., Lombardi, A. M., Chiarabba, C., & Montuori, C. (2012).
 930 Heterogeneities along the 2009 L'Aquila normal fault inferred by the b-value distribution.
 931 *Geophysical research letters*, *39*(15).
 932
- 933 Herrmann, M., & Marzocchi, W. (2021). Inconsistencies and lurking pitfalls in the magnitude–
 934 frequency distribution of high-resolution earthquake catalogs. *Seismological Society of*
 935 *America*, *92*(2A), 909-922.
 936
- 937 Sukan, M., Kato, A., Miyake, H., Nakagawa, S., & Vuan, A. (2014). The preparatory phase of the
 938 2009 Mw 6.3 L'Aquila earthquake by improving the detection capability of low-magnitude
 939 foreshocks. *Geophysical Research Letters*, *41*(17), 6137-6144.
 940